THESIS FOR THE DEGREE OF LICENTIATE OF ENGINEERING

in

Thermo and Fluid Dynamics

Large Eddy Simulation of clearings in forest and their effect on wind turbines

by

JOHANNA MATSFELT

Department of Mechanics and Maritime Sciences
CHALMERS UNIVERSITY OF TECHNOLOGY
Gothenburg, Sweden, 2018

Large Eddy Simulation of clearings in forest and their effect on wind turbines
JOHANNA MATSFELT

© JOHANNA MATSFELT, 2018

THESIS FOR LICENTIATE OF ENGINEERING No. 2018:12

Department of Mechanics and Maritime Sciences
Chalmers University of Technology
SE-412 96 Gothenburg
Sweden
Telephone +46-(0)31-7721000

This document was typeset using LaTeX

Printed at Chalmers Reproservice
Gothenburg, Sweden, 2018

Large Eddy Simulation of clearings in forest and their effect on wind turbines

JOHANNA MATSFELT

johanna.matsfelt@chalmers.se
Department of Mechanics and Maritime Sciences
Chalmers University of Technology

Abstract

When the number of wind farms increases, the number of wind turbines placed in forested areas will also increase, this is because of the large forest areas in Sweden. When the wind turbines are placed in forested areas the fatigue loads increase drastically, so their maintenance costs increase making them less profitable. In this work clearings in forest are studied to be able to increase the electrical power generated by the wind turbines and decrease the fatigue loads to make them more profitable.

The approach in this work is to use Computational Fluid Dynamics (CFD) with the Large Eddy Simulation (LES) turbulence model coupled to an aero elastic solver that solves the dynamic response of the wind turbine.

Here Ryningsnäs in Sweden is investigated with a homogeneous forest, the current clearing and an extended clearing. The electrical generator power was highest for the current clearing. But the fatigue loads were both higher and lower than the homogeneous forest depending on which part of the wind turbine that was investigated. The extended clearing nearly always had the lowest fatigue loads but unfortunately also the lowest electrical generator power. Further optimization of the clearings and the wind turbine locations in relation to them is needed to find the sweet spot where the fatigue loads are lower and the electrical generator power is higher.

Keywords: ALM, CFD, FAST, forest clearing, LES, OpenFOAM, SOWFA, Wind turbine.

”Normal people... believe that if it ain’t broke, don’t fix it. Engineers believe that if it ain’t broke, it doesn’t have enough features yet.” - Scott Adams

Acknowledgments

I would like to express my gratitude to my supervisor Lars Davidson for the opportunity to carry out this work and dive deep into the ocean of CFD and programming. I would also like to thank my co-supervisor Håkan Nilsson for being there for OpenFOAM related questions. A big thank you to Johannes Derneryd at Stena Renewable and Kyle Brennan at Meventus for always sharing their knowledge about wind turbines and drive to move the project forward.

I would also like to thank Sara Fogelström and Ola Carlson at SWPTC and the staff at the fluid dynamics division for their support. Many thanks to my colleagues at C3SE at Chalmers for sharing their knowledge about high performance computing with me and for interesting discussions.

Finally I would like to thank my family for their support and always letting me develop my interests.

This project was financed through the Swedish Wind Power Technology Centre (SWPTC), Stena Renewable and Meventus. SWPTC is a research centre for design of wind turbines. The purpose of the centre is to support Swedish industry with knowledge of design techniques as well as maintenance in the field of wind power. The focus is foremost on developing turbine design which minimises the costs for production and maintenance of turbines. The Centre is funded by the Swedish Energy Agency, Chalmers University of Technology as well as academic and industrial partners.

Johanna Matsfelt, Göteborg, May 2018

Nomenclature

Greek symbols

α	Wind turning angle
γ	Extinction coefficient of light
Ω	Rotation rate vector at a location on the planetary surface
ω	Planetary rotation rate
ϕ	Latitude
ρ	Air density
ρ_0	Reference air density
τ_{ij}^D	Sub grid stress tensor
θ	Potential temperature
θ_0	Reference potential temperature
ε	Permutation tensor
ε_{1D}	1D Gaussian distribution width
ε_{2D}	2D Gaussian distribution width
ε_{3D}	3D Gaussian distribution width
ε_i	Parameter to control the Gaussian distribution width

Symbols

$\bar{u}_i$	Velocity component in the x_i-direction
$\Delta\theta$	Tangential local cell length
Δr	Tangential radial cell length
Δx	Axial local cell length
A_c	Downward cumulative leaf area index (LAI)
a_f	Vertical leaf area density
B	Number of blades on the wind turbine
c	Local chord length
C_D	Local drag coefficient
C_L	Local lift coefficient
C_{Df}	Forest drag coefficient
D_i^{ADM}	Actuator Disk drag force
D_i^{ALM}	Actuator Line drag force
e_D	Unit vector in the direction of the drag
e_L	Unit vector in the direction of the lift
f_i^T	Forces from the actuator turbine model
F_i^{ADM}	Actuator Disk element force
F_i^{ALM}	Actuator Line element force

F_i^A	Force field projected to the CFD cells
F_i^T	Actuator element force
$F_{f,i}$	Forest drag
h	Forest height
L_i^{ADM}	Actuator Disk lift force
L_i^{ALM}	Actuator Line lift force
L_m	Maximum value of the leaf area density
n	Parameter that controls the shape of the vertical leaf area density
p_{1D}	Axial distance between the actuator point and the cell
p_{2D}	Distance between the actuator point and the cell with the same radii
Q_h	Canopy top heat flux
q_j	Sub grid heat flux
R	Rotor radius
r	Distance between the actuator point and the cell
r	Local radius to the center location on the area section
S_h	Canopy heat source term
U	Local wind speed
U_{rel}	Local relative velocity
z_m	z location where the maximum value of the leaf area density occur

Abbreviations

ADM	Actuator Disk Model
ALM	Actuator Line Model
BEM	Blade Element Momentum Method
CFD	Computational Fluid Dynamics
FAST	Fatigue, Aerodynamics, Structures, and Turbulence code
LAI	Leaf area index
LES	Large Eddy Simulation
NREL	National Renewable Energy Laboratory
RMS	Root mean square
SOWFA	Simulator fOr Wind Farm Applications
SWPTC	Swedish Wind Power Technology Centre

Contents

Chapter 1

Theory

1.1 Forest and wind turbines

In Sweden the large resource of forest compared to non-forested areas will cause that many wind turbines will be placed in a forested region. Previous research has shown that the turbulence and wind shear are increased drastically by the influence of the forest. It has been shown that a wind turbine located in a homogeneous forest will experience a more extreme situation than covered by the IEC design criteria [1]. When maintenance logs of wind turbines in forest and non-forested areas where compared, the wind turbines located in the forest showed 2.2 times more fault duration in a year and the frequency of maintenance increased by 20% [2].

1.2 Clearings in forest regions

When a forest edge is present the flow field is changed dramatically compared to a fully homogeneous forest. Large Eddy Simulation (LES) of a forest edge flow has been made in [3] and compared to results using static inlet boundary condition and dynamic inlet boundary condition from a precursor simulation. The dynamic inflow condition outperformed the static and the recommendation was that the static inflow condition should be avoided [3]. Measurements with wind from an open landscape meeting a forest edge has been performed in [4]. The data where taken at 1.5 forest heights inside the forest at leaf-off and leaf-on with leaf area index of (LAI) of 1 and 6 respective. The total kinetic energy was generally higher during the leaf-on period than at the leaf-off period. The reason was assumed to be the higher roughness of the upstream landscape during this period. In both cases the total kinetic energy was unchanged when the flow moved over the forest edge and to the measurement location. The momentum flux was largest at the open landscape location which is somewhat surprising. When comparing these measurements with simulation performed, where a flow is meeting a forest edge and developing over the forest for two forest cases with LAI of 2 and 5 [5]. The simulation results agree with the trends in the measurements at 1.5 forest heights inside the forest. But in the simulation more information can be provided when the flow is developing further along the forest. In both forest types the total kinetic energy and the momentum flux are increased as the flow is moving along the forest, with the highest LAI forest showing the highest values of the two. The distance from the forest edge

that the flow is affected was studied and results showed that edge effects were significant about 22 forest heights after the edge [6]. The affected distance could be even larger for scalar quantities such as temperature because they need a larger distance than the velocity to adjust [7]. The large effecting distance after the forest edge show that forests with clearings streamwise larger than five forest heights will always show edge effects. This is due to the formation of a sub-canopy wind jet at the leading edge in forests with clearings [8]. When the clearing is in the form of a lake, it has been shown that the turbulent mixing was mostly due to the wind shear at the three height of the canopy rather than the thermal stratification due to the lake [9].

1.3 Forest in complex terrain

When comparing computations assuming horizontal homogeneous forest to measurements the wind profiles seemed to agree but the third order moment showed that there may be some terrain dependence [10]. This showed that further studies are needed to find the dependency of the turbulence in the forest on the complex terrain it is located in. When LES where compared to wind tunnel experiments of the flow over a forested 2D hill [8], the validation showed that the model could accurately reproduce the flow characteristics. In [11] the k-ε turbulence model was used to perform 2D and 3D simulation of a forested park damaged by a windstorm. From the 2D simulations it was observed that a region of turbulence always develops at a distance from the leading edge of the forest but the distance depends on the heterogeneity of the forest. If the forest is heterogeneous both vertically and horizontally the strong wind shear at the top of the canopy is weakened and thereby also the turbulence region caused by it compared to a homogeneous forest. The simulations also showed that the intensity of the turbulence increased when the forest was denser during the summer i.e. high LAI values. From the 3D simulations of this specific forest the level of the turbulence was more dependent to the forest leading edge since the forest was larger allowing the wind shear and thereby also the turbulence to grow along a larger distance. The simulations could point out the regions of the strongest turbulence levels and these seemed to agree with the damaged areas. This also showed that the damage in the forest was due to the wind characteristics. This assumption was also strengthened by a study that the damage could not be consistent with any other environmental factor. The authors pointed out that the physics of the model could not provide information about any instantaneous turbulent quantities. They also showed a strong interest in simulating turbulent flow in complex terrain over a strongly heterogeneity forest.

1.4 Forest modelling

The forest can be modelled on many ways. One example is to represent it by the roughness of the wall model [12]. A more complex way is to simulate it by using a drag and heat source as has been done here [13].

$$F_{f,i} = -C_{Df} a_f U \bar{u}_i \tag{1.1}$$

Eq. 1.1 shows the addition to the momentum equation i.e. the drag force of the forest. C_{Df} is the drag force coefficient of the forest and it is set to 0.15 [13]. The vertical leaf area density a_f

is supposed to simulate the shape of the drag force of the simulated forest. An illustration can be seen in fig. 1.1.

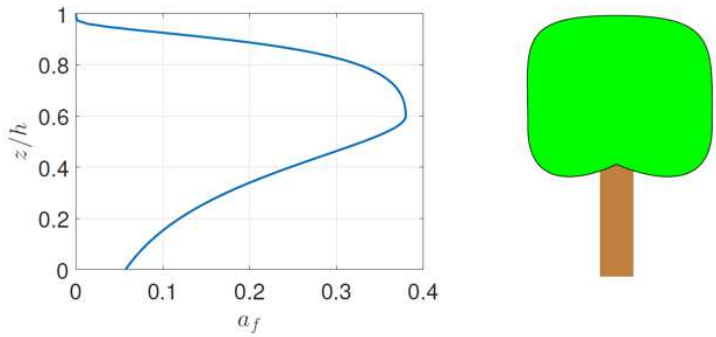

Figure 1.1: Example of the vertical leaf area density profile

The heat source in the potential temperature equation is computed in eq. 1.2. To represent the heat source in the forest γ is the extinction coefficinet of light set to 0.6 [13]. The canopy heat source Q_h is dependent on which kind of atmospheric stability is simulated.

$$S_h = \frac{\partial}{\partial z}(Q_h exp(-\gamma A_c)) \tag{1.2}$$

The area leaf density seen in eq. 1.2 is evaluated using eq. 1.3. It is the total vertical leaf density of the forest. The vertical leaf area density a_f can be obtained in numerous ways. One way is to measure it in the forest. Another way that has been used here is to obtain it from an empirical formula [14].

$$A_c = \int_z^h a_f dz \tag{1.3}$$

In eq. 1.4 the shape of the forest is determined by the n, L_m and z_m parameters. The n parameter has been evaluted in different ways by the developers and eq. 1.5 has been shown to properly evaluate n [14]. The L_m and z_m parameters on the other hand are dependent on which kind of forest that is evaluated [13, 14].

$$a_f(z) = L_m \left(\frac{h-z_m}{h-z}\right)^n exp\left(n\left(1-\left(\frac{h-z_m}{h-z}\right)\right)\right) \tag{1.4}$$

$$n = \begin{cases} 6 & 0 \leq z < z_m, \\ \frac{1}{2} & z_m \leq z \leq h \end{cases} \tag{1.5}$$

1.5 Actuator turbine models

When simulating wind turbines in CFD actuator turbine models are often used in favour of solving the flow field over each blade. The main advantage of this is that the boundary layer on each blade does not need to be resolved so the mesh resolution can be reduced significantly [15]. In actuator

turbine models the wind turbine is simulated by lift and drag forces. They are calculated using C_L and C_D from 2D airfoil tables and assuming constant cord length of each section of the blades. But the way the blades are modelled could vary in numerous ways e.g. as disk in Actuator Disk Model (ADM) and as lines in an Actuator Line Model (ALM) illustration seen in fig. 1.2.

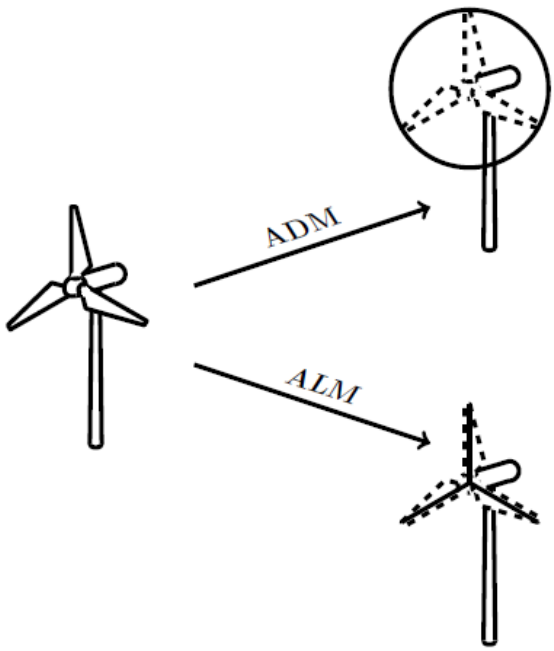

Figure 1.2: Simulation of wind turbine blades in ADM and ALM

1.5.1 Actuator disk model

The ADM is based on the Blade Element Momentum Method (BEM) which calculates the forces on the blades modelled as 2D airfoil profiles. The blades are here simulated as a disk.

$$F_i^{ADM} = \left(L_i^{ADM}, D_i^{ADM}\right) = \frac{B}{2\pi r}\frac{1}{2}\rho U_{rel}^2 c\left(C_L e_L, C_D e_D\right) \tag{1.6}$$

In ADM the lift and drag forces are per unit area as can be seen in eq. 1.6 as L_i^{ADM} and D_i^{ADM}. An example of an area section where the force from an ADM routine could be applied on can be seen in fig. 1.3. Eq. 1.6 is a modified lift and drag force formula of an airfoil. Further information on the steps from BEM to ADM can be found in [16]. Since the ADM simulates the wind turbine blades as a disk the flow will be axisymmetric.

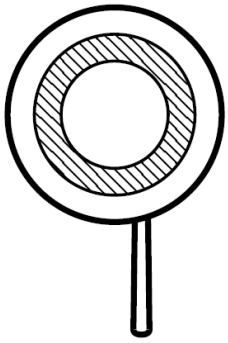

Figure 1.3: Area sections of ADM

1.5.2 Actuator line model

In ALM the blades are simulated as lines. This representation makes it not possible to run the simulation axisymmetric as in ADM. With ALM a 3D simulation is needed.

$$F_i^{ALM} = \left(L_i^{ALM}, D_i^{ALM}\right) = \frac{1}{2}\rho U_{rel}^2 c \left(C_L e_L, C_D e_D\right) \tag{1.7}$$

The ALM formula for lift and drag can be seen in eq. 1.7, as L_i^{ALM} and D_i^{ALM}. Compared to the ADM the ALM formula has unit force per meter instead of force per area. ALM can capture the tip and root vortices which ADM cannot [17]. To have a representation of these vortices are important when studying the near wake and is a clear advantage of the ALM over the ADM. The advantage of ADM compared to ALM is the speed of convergence. This is because the actuator lines of ALM should not travel through too many cells each time step, preferably only on cell. Hence the time step must be much smaller than what can be used in ADM.

1.6 Coupling actuator turbine models and CFD

Actuator turbine models can be used in CFD in two ways. The first one is called one way coupling where the flow field of the CFD is fed in to the actuator turbine model and evaluated. The second way is to feed the forces obtained by the actuator turbine model back to the CFD, this is called two way coupling. To do this a Gaussian distribution is used to smear the force in the neighborhood of the actuator point. This is necessary in order to avoid numerical oscillations in the simulation that otherwise will occur [12]. The way the forces in the Gaussian is smeared in the neighborhood of the actuator point can be done in numerous ways. In ADM a 1D Gaussian with distribution smearing in the axial direction is recommended [16]. The physical representation of this can be seen fig. 1.4

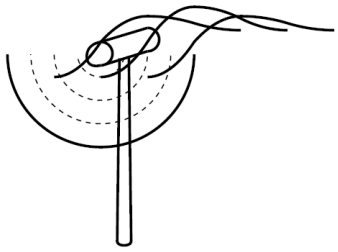

Figure 1.4: Physical representation of a 1D Gaussian distribution in the streamwise direction used together with ADM

In eq. 1.8 an example of a 1D Gaussian distribution can be seen.

$$F_i^T(p_{1D}) = \frac{F_i^A}{\varepsilon_{1D}^3\sqrt{\pi}} exp\left[-\left(\frac{p_{1D}}{\varepsilon_{1D}}\right)^2\right] \tag{1.8}$$

In this 1D smearing ε_{1D} is described by eq. 1.9. ε_i is recommended a value from 1 to 4 [16].

$$\varepsilon_{1D} = \varepsilon_i \Delta x \tag{1.9}$$

A 2D or 3D Gaussian distribution is usually used together with ALM. A 2D Gaussian distribution will not only smear the force in the axial direction but also in the azimuthal direction following a constant radius. So the force will not only be applied to the flow axially as in fig. 1.4 but also in azimuthal direction in the rotor plane as shown in fig. 1.5.

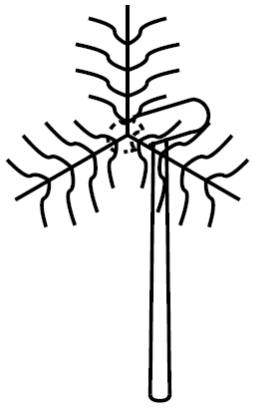

Figure 1.5: 2D Gaussian distribution in addition to 1D Gaussian also apply forces in the rotor plane.

A 2D Gaussian distribution can be seen in eq. 1.10. The variable p_{2D} is the distance from the actuator point to the node on the line with the same radius.

$$F_i^T(p_{2D}) = \frac{F_i^A}{\varepsilon_{2D}^3\pi} exp\left[-\left(\frac{p_{2D}}{\varepsilon_{2D}}\right)^2\right] \tag{1.10}$$

The ε_{1D} in ADM is now not only a variable depending on the axial mesh resolution but the whole 3D mesh resolution and therefor renamed to ε_{2D}. Eq. 1.11 shows the recommended formula for ε_{2D} [16].

$$\varepsilon_{2D} = \varepsilon_i \sqrt{(R\Delta\theta^2)\,\Delta r^2 \Delta x^2} \tag{1.11}$$

A 3D Gaussian distribution can also be used. The force is then also applied along the radial direction of the actuator lines. This can physically be seen as spheres that increase in intensity the closer to the actuator point the cell is. The 3D Gaussian smears the force over the acual tip of the wind turbine blade. So when the tip flow behavior has been investigated a 2D gaussian distribution has been preferred instead [16]. A 3D Gaussian distribution in shown in eq. 1.12 [18].

$$F_i^T(r) = \frac{F_i^A}{\varepsilon_{3D}^3 \pi^{3/2}} exp\left[-\left(\frac{r}{\varepsilon_{3D}} \right)^2 \right] \tag{1.12}$$

The ε_{3D} has been recommended to be twice the cell axial length near the actuator line [15]. Independent of which Gaussian distribution that is choosen, the choice of ε and cell size has been shown to have an impact on the results and have to be choicen with care [12, 16, 17, 19, 20].

1.7 SOWFA by NREL

The Simulator fOr Wind Farm Applications (SOWFA) developed by National Renewable Energy Laboratory (NREL) has been used throughout this work [12]. SOWFA is a CFD solver that link the FAST version 7 code which is an aero elastic solver developed by NREL to OpenFOAM that models the wind. This is done by replacing the momentum part of the BEM theory in FAST by CFD. FAST evaluates the structural and system response of the wind turbine and sends the aerodynamic forces back to the CFD. So SOWFA is based on two way coupling between OpenFOAM and FAST.

The transport equation for momentum used in SOWFA can be seen in eq. 1.13. The reference potential temperature θ_0 is set to 300K. The two last terms are the actuator turbine model and the forest model contributions.

$$\frac{\partial \bar{u}_i}{\partial t} + \frac{\partial}{\partial x_j}\left(\bar{u}_j \bar{u}_i\right) = -2\varepsilon_{i3k}\Omega_3 \bar{u}_k - \frac{\partial \tilde{p}}{\partial x_i} - \frac{1}{\rho_0}\frac{\partial}{\partial x_i}\bar{p}_0(x,y) - \frac{\partial}{\partial x_j}\left(\tau_{ij}^D\right) - g\left(\frac{\bar{\theta}-\theta_0}{\theta_0}\right)\delta_{i3} + \frac{1}{\rho_0} f_i^T + F_{f,i} \tag{1.13}$$

SOWFA includes the Coriolis force seen in eq. 1.13. The rotational rate vector at a location on the planetary surface is evaluated by eq. 1.14.

$$\Omega_j = \omega \begin{bmatrix} 0 \\ \cos\phi \\ \sin\phi \end{bmatrix} \tag{1.14}$$

The transport equation of the potential temperature can be seen in eq. 1.15. The last term is the heat source in the forest model.

$$\frac{\partial \bar{\theta}}{\partial t} + \frac{\partial}{\partial x_j}\left(\bar{u}_j \bar{\theta}\right) = -\frac{\partial}{\partial x_j}\left(q_j\right) + S_h \tag{1.15}$$

SOWFA can only use LES as turbulence model. The sub grid filter model is the Smagorinsky model [21]. The wall model was developed by Schumann [22]. The ALM model is used as actuator turbine model with a 3D Gaussian distribution function.

The work flow with SOWFA is to first run an atmospheric boundary layer simulation without any wind turbines and using only cyclic boundary condition. This is called a precursor simulation. When the flow is considered to be fully developed, planes in the computation domain are saved. These are later used as inlet boundary condition in the simulation that includes wind turbines. The main advantage with this procedure is that the flow is fully developed at the inlet in the wind turbine simulation. In the following simulations the wind turbine are introduced and OpenFOAM is coupled to FAST. In this work the data obatined from FAST are processed using the rain flow counting algorithm to obtain the fatigue loads [23].

Chapter 2

Results

To be able to validate and investigate the implementations in SOWFA the test site of Ryningsnäs is used.

2.1 Ryningsnäs

The Ryningsnäs test site is simulated with wind blowing from the south. The wind turbine after the clearing is located within 22 forest heights after the clearing which is the forest effecting distance [6]. The computational domain seen from above can be seen to the left in fig. 2.1. Here the forest is in white and the clearing in grey, also seen is the locations of the two wind turbines at the site. In all the simulations the 5MW wind turbines from NREL is used [24]. To be able to draw any general conclusions of the shape of the clearing and its effects on the wind turbines one more clearing is investigated. This clearing has the maximum width of the current clearing along it and reaches until the second turbine. This clearing is called the extended clearing and can be seen to the right in fig. 2.1. Both the clearings are streamwise larger than five forest heights, which has been shown that leads to that the flow always show edge effects [8]. To be able to distinguish the effects of the clearings a setup with homogeneous forest is also investigated and its domain can be seen in the middle of fig. 2.1. All the computational domains has a width (y direction) of 1000m, a length (x) of 1600m and a height (z) of 800m.

The forest has a height of 20m and is modelled using the model by Shaw and Shumann see eq. 1.1, 1.2. The forest at the Ryningsnäs site is made up of scots pine tree and it is used to model the vertical area density [14]. The setup uses z_m of $0.6h$ and L_m of 0.37 to simulated scots pine three [13, 14]. The wall model was set to model grass plains below the forest.

The simulations was set to simulate neutral stratification. All the computational domains was first simulated without any wind turbines. In order to investigate the flow field when it is disrupted only by the clearings. These results are validate against data from an extensive measurement campaign performed at Ryningsnäs [25]. Some difference to the measurements are expected since the simulations only take into account wind blowing from the south. Then the second wind turbine after the clearing was added, to find the effects the clearings had on this turbine. Finally both the turbines were in the simulations, where the wake of the first wind turbine could affect the second wind turbine.

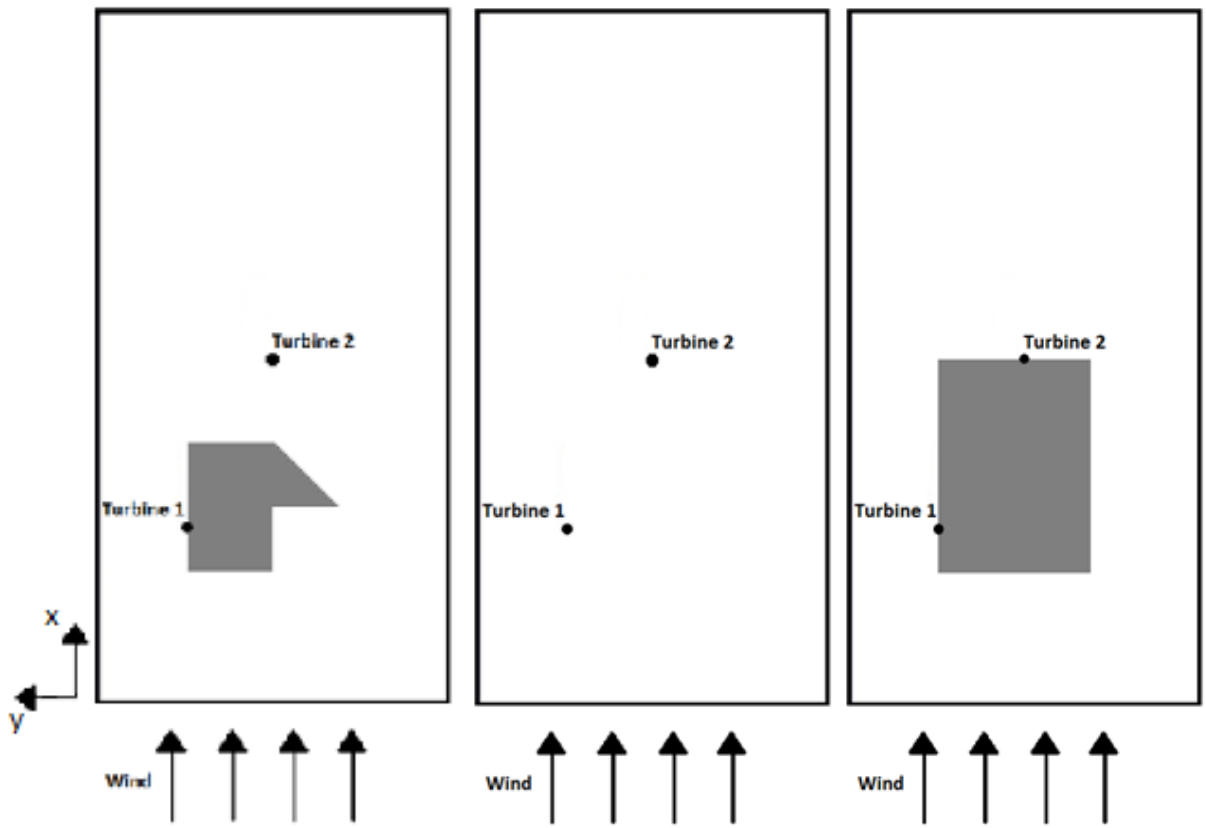

Figure 2.1: Current, Homogeneous and Extended computational domains, white is forest and clearing in grey, the locations of the two wind turbines are shown with black bullets.

2.1.1 Precursor simulation

As inlet boundary condition, y-z planes from a precursor simulation is used. The precursor simulation is set to have 10m/s at hub height of the wind turbines at 90m. All the simulations are using the width of 1000m and height of 800m of the computational domains. The length is investigated to avoid streaks. The time averaged $\bar{u}$ velocity planes at hub heigth for the computational domain length of 1600m, 3000m, 5000m and 10000m can be seen in fig. 2.2. For the two shortest computational domains streaks are clearly seen, which means that the flow is affected by the short computational domain. The 3000m setup is the shortest length recommended for SOWFA at neutral to lightly unstable stratifications [12]. For this setup with neutral stratification the 3000m computational domain is not enough. In the simulations using the two longest computational domains no streaks are seen so both are accepted to be used for creating inlet boundary condition. But the 5000m precursor simulation is chosen as inlet boundary condition because of its lower computational cost.

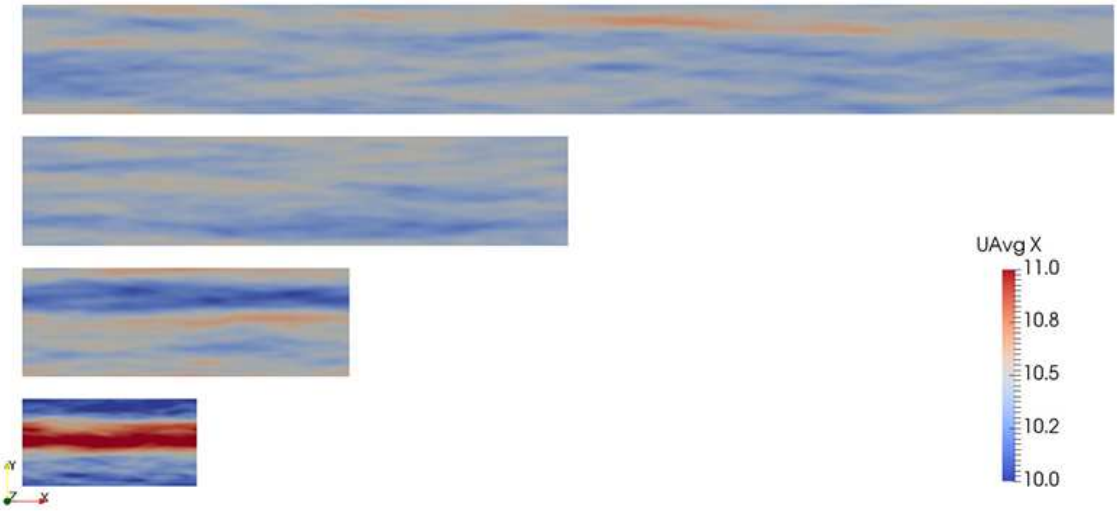

Figure 2.2: Planes of the time averaged $\bar{u}$ velocity for the precursor simulations at hub height.

Despite the need to be careful with the length chosen for the precursor simulation in order to avoid streaks. This kind of dynamic inflow boundary condition was found to be much better than a static inlet boundary condition in LES simulations of an edge flow [3].

2.1.2 Atmospheric boundary layer simulations

No wind turbines are included in the simulations in this section. To investigate the flow field x-z planes at $y = 400m$ of each computational domain is chosen for the analysis. The $\bar{u}$ velocity is shown in fig. 2.3, $\bar{v}$ velocity in fig. 2.4 and $\bar{w}$ velocity in fig. 2.6. The homogeneous forest is located in the middle of each figure and as expected the wind is blowing along the forest with a constant boundary layer height. The $\bar{u}$ velocity is increasing close to the ground in the downstream part of the extended clearing. In the current clearing the flow is not affected as much by the clearing as in the extended clearing. After the clearings the flow on top of the forest is accelerating seen by that the white contour line is moving closer to the ground. The flow is then starting to build a new boundary layer above the forest.

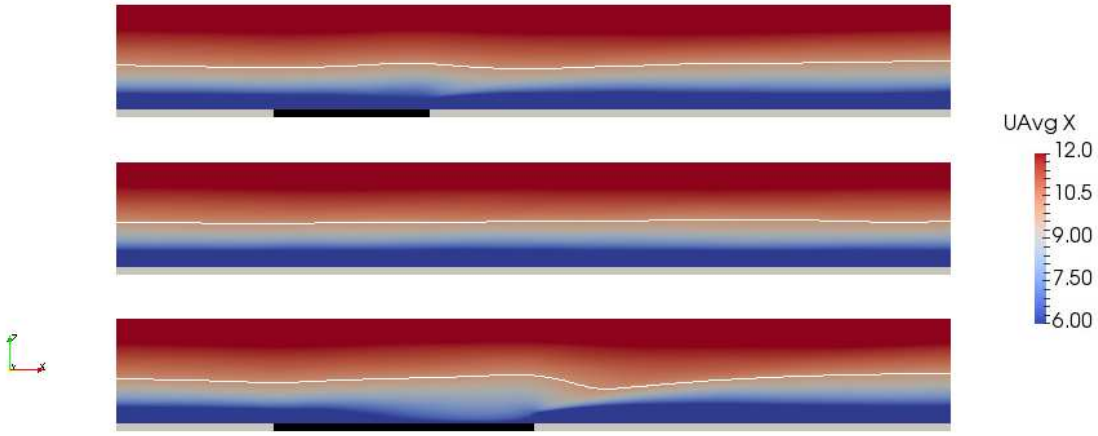

Figure 2.3: Time averaged $\bar{u}$ velocity in atmospheric boundary layer simulations on plane at y of 400m. Contour line in white shows time averaged $\bar{u}$ velocity of 10m/s. From the top current clearing, homogeneous forest and extended clearing. Below each plane the location of the clearing is marked in black.

The $\bar{v}$ velocity is mainly affected in the case of the current clearing when looking at x-z planes at $y = 400m$. The reason is that this plane is cutting just at the edge of the clearing. In the end of the current clearing the flow is also moving more to the east (negative $\bar{v}$) than what is seen in the case of the extended clearing.

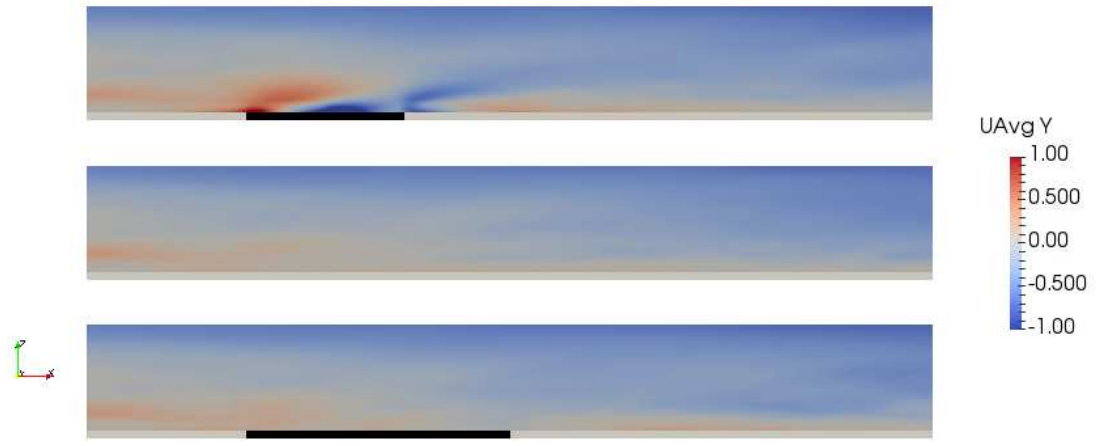

Figure 2.4: Time averaged $\bar{v}$ velocity in atmospheric boundary layer simulations on x-z plane at y of 400m. From the top current clearing, homogeneous forest and extended clearing. Below each plane the location of the clearing is marked in black.

The locations of the wind turbines are studied in more detail by looking at the horizontal velocity ($U_l = \sqrt{\bar{u}^2 + \bar{v}^2}$) normalized by the friction velocity ($u_* = \langle \overline{u'v'}^2 + \overline{v'w'}^2 \rangle^{1/4}$) evaluated at two forest heights seen in fig. 2.5. The velocity at the first wind turbine is more or less the same in all the simulations. This is not that surprising since the flow has mainly travelled along

homogeneous forest before reaching this wind turbine. For the location of wind turbine 2 the homogeneous forest and the current clearing show the same velocity at the bottom and top of the rotor plane. But the homogeneous forest has a more flat velocity profile in between. The wind turbine after the clearing in the extended clearing has the highest velocity at the bottom of the rotor plane and the lowest velocity at the top of the rotor plane. Hence this wind turbine location has the flattest velocity profile of them all i.e. the lowest wind shear.

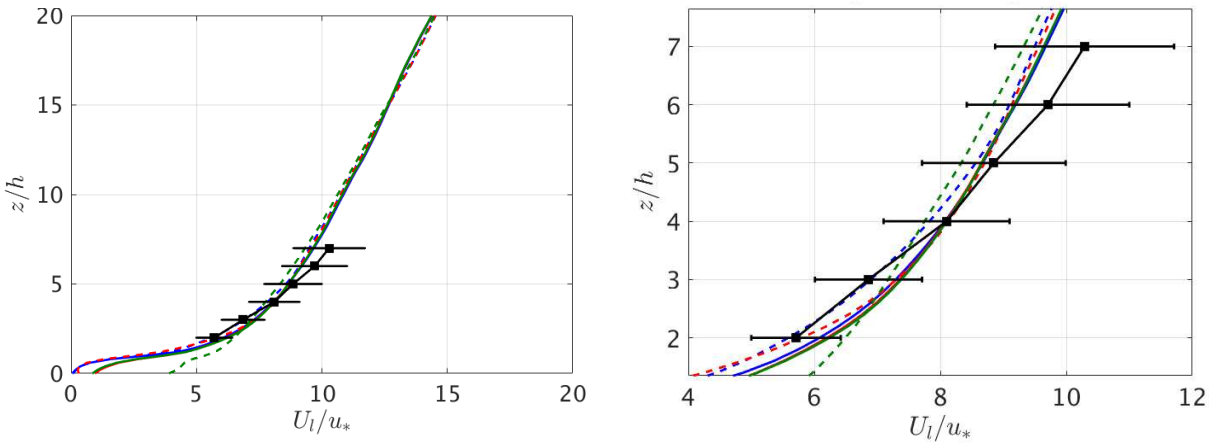

Figure 2.5: $\langle U_l/u_* \rangle$ from atmospheric boundary layer simulations at location of the wind turbine to the left and a zoom in rotor plane to the right. —: Wind turbine 1 in homogeneous forest, - -: Wind turbine 2 in homogeneous forest, —: Wind turbine 1 in current clearing, - -: Wind turbine 2 in current clearing, —: Wind turbine 1 in extended clearing, - -: Wind turbine 2 in extended clearing, —■—: Measurements

When looking at the $\bar{w}$ velocity in fig. 2.6 the flow is moving downwards into the clearing after the forest edge and upwards after the clearings. This velocity is the strongest in the case of the extended clearing because the clearest disrupting of the forest boundary layer before the clearing is seen here. This is consistent with what is observed for the $\bar{u}$ velocity.

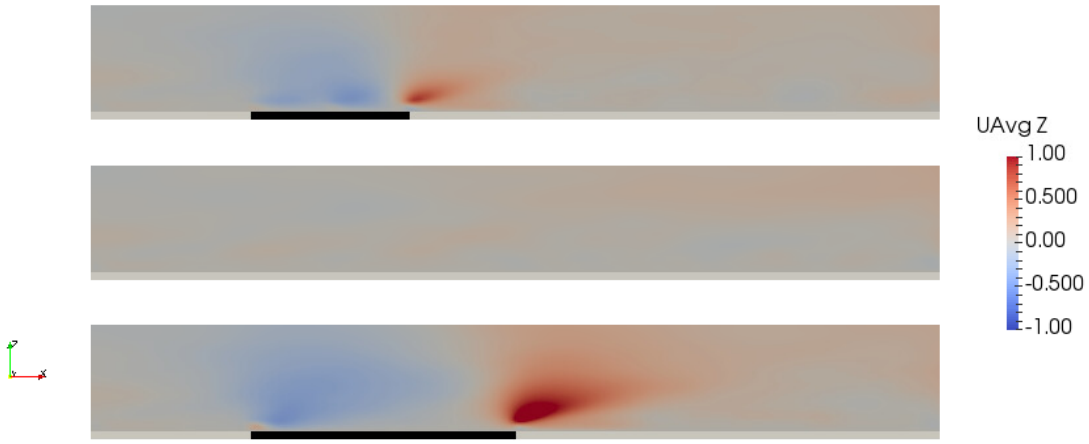

Figure 2.6: Time averaged $\bar{w}$ velocity from the atmospheric boundary layer simulations on a x-z plane at y of 400m. From the top current clearing, homogeneous forest and extended clearing. Below each plane the location of the clearing is marked in black.

The vertical momentum flux along the streamwise direction can be seen in fig. 2.7. In the rotor plane all the forest types for wind turbine 1 are very similar. Inside the forest the extended forest shows a bit higher vertical momentum flux than the other cases. This is probably due to the larger clearing surrounding this wind turbine in the extended clearing. For the location of wind turbine 2, the homogeneous forest has the highest vertical momentum flux and the current clearing the lowest. The vertical momentum flux for the extended clearing has a different shape and decreases a lot at four forest heights. This is because the flow has adapted to the clearing. Wind turbine 2 in the current clearing is the one that should be closest to the measurements and it is within acceptable margin.

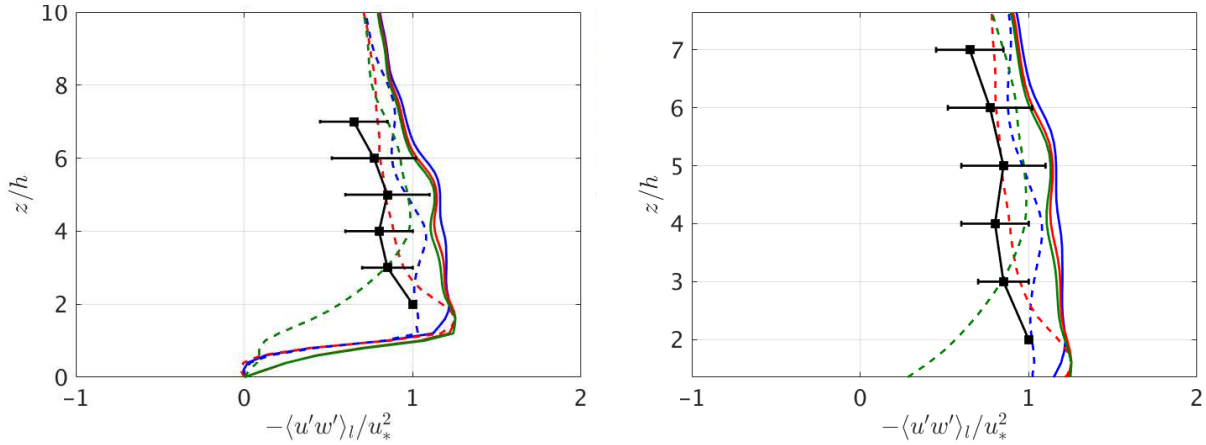

Figure 2.7: $-\langle u'w'/u_*^2\rangle$ from atmospheric boundary layer simulations at location of the wind turbine to the left and a zoom in rotor plane to the right. —: Wind turbine 1 in homogeneous forest, – –: Wind turbine 2 in homogeneous forest, —: Wind turbine 1 in current clearing, – –: Wind turbine 2 in current clearing, —: Wind turbine 1 in extended clearing, – –: Wind turbine 2 in extended clearing, —■—: Measurements

The variance of the $\bar{u}$ velocity can be seen in fig. 2.8, for the $\bar{v}$ velocity in fig. 2.9 and for the $\bar{w}$ velocity in fig. 2.10. $\langle u'u'/u_*^2 \rangle$ is the largest of them all. For wind turbine 1 the current and extended clearing are similar, the homogeneous forest is a bit higher along the rotor location and a bit lower below. For wind turbine 2 the trends are the same as for $-\langle u'w'/u_*^2 \rangle$.

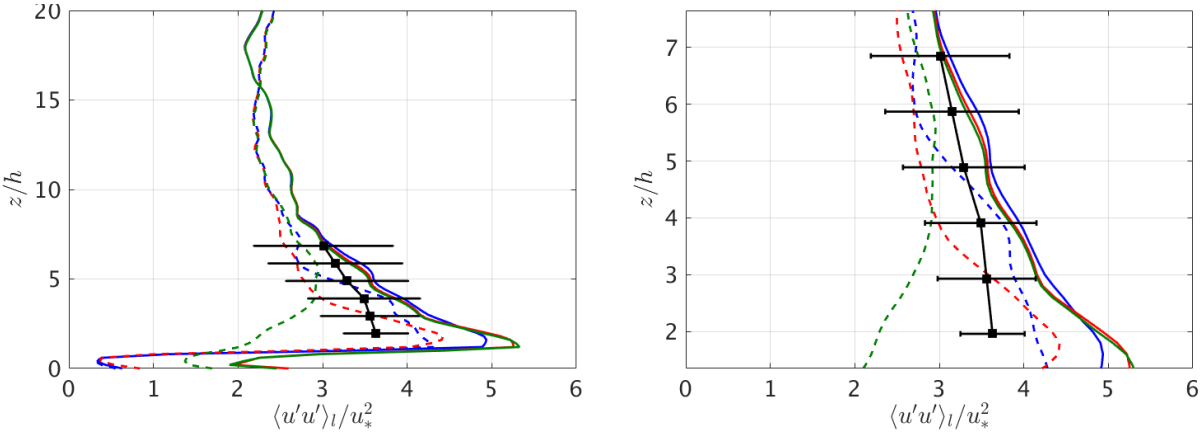

Figure 2.8: $\langle u'u'/u_*^2 \rangle$ from atmospheric boundary layer simulations at location of the wind turbine to the left and a zoom in rotor plane to the right. —: Wind turbine 1 in homogeneous forest, - - : Wind turbine 2 in homogeneous forest, —: Wind turbine 1 in current clearing, - - : Wind turbine 2 in current clearing, —: Wind turbine 1 in extended clearing, - - : Wind turbine 2 in extended clearing, —■—: Measurements

For $\langle v'v'/u_*^2 \rangle$ at the location of wind turbine 1 the trends are the same as for $-\langle u'w'/u_*^2 \rangle$ but with lower magnitudes. In the upper part of the rotor location all the cases are very similar. But in the lower part and close to the ground the results differ a lot. Wind turbine 2 in the homogeneous forest shows values close to wind turbine 1 in the homogeneous forest and wind turbine 2 in the current clearing has a bit lower magnitude but the same shape. But the shape at wind turbine 2 for the extended clearing is the lowest of them all in the lower region of the rotor location but it is then not decreasing as much as the other cases in the forest region. The reason is probably because the wind has here adapted to the longer clearing and thereby the effect of the forest can no longer be seen.

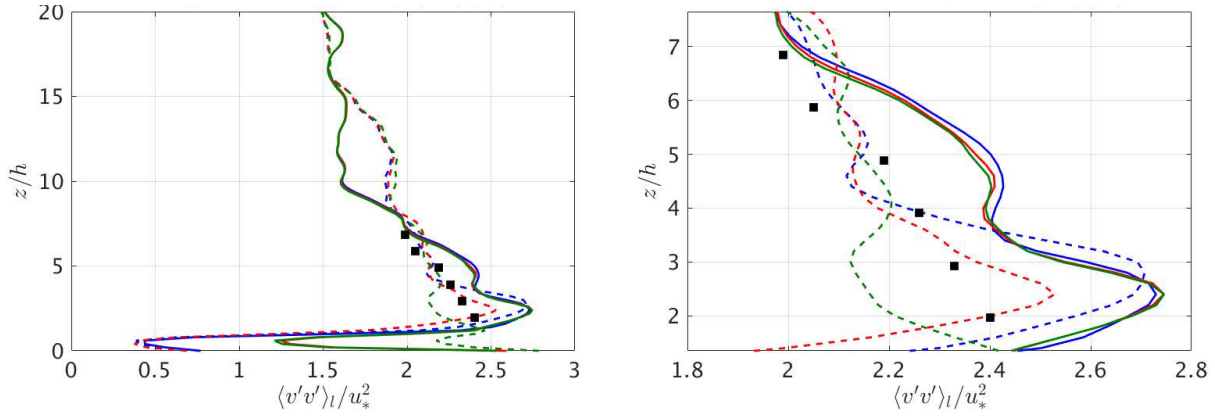

Figure 2.9: $\langle v'v'/u_*^2\rangle$ from atmospheric boundary layer simulations at location of the wind turbine to the left and a zoom in rotor plane to the right. —: Wind turbine 1 in homogeneous forest, - -: Wind turbine 2 in homogeneous forest, —: Wind turbine 1 in current clearing, - -: Wind turbine 2 in current clearing, —: Wind turbine 1 in extended clearing, - -: Wind turbine 2 in extended clearing, —■—: Measurements

Within the forest all the simulations predict the same $\langle w'w'/u_*^2\rangle$ profile seen in fig. 2.10. For wind turbine 1 in the rotorplane the homogeneous forest has the highest values followed by the current clearing and the extended clearing. The second wind turbine in the homogeneous forest is the only one that has similar shape as the measurements. For wind turbine 2 the highest values are seen for the extended clearing, but the magnitude is lower than both $\langle u'u'/u_*^2\rangle$ and $\langle v'v'/u_*^2\rangle$.

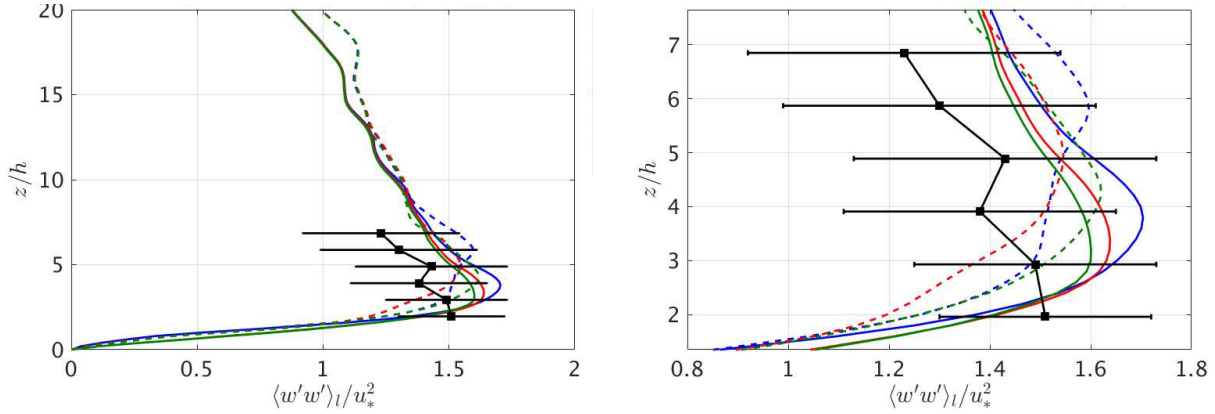

Figure 2.10: $\langle w'w'/u_*^2\rangle$ from atmospheric boundary layer simulations at location of the wind turbine to the left and a zoom in rotor plane to the right. —: Wind turbine 1 in homogeneous forest, - -: Wind turbine 2 in homogeneous forest, —: Wind turbine 1 in current clearing, - -: Wind turbine 2 in current clearing, —: Wind turbine 1 in extended clearing, - -: Wind turbine 2 in extended clearing, —■—: Measurements

The turning angle can be seen in fig. 2.11. It is defined as positive when the flow is moving west. Ryningsnäs is located on the northern hemisphere and due to this, the Coriolis force will deflect the wind to the west which agrees to what is predicted by all the simulations. Wind turbine 1 is located at the edge of the forest edge in the current and extended clearing. Along the

rotor location it can be seen that this will cause the wind to deflect more to the west i.e. more towards wind turbine 2 than in the homogeneous forest. For the location of wind turbine 2 the homogeneous forest and the extended clearing have a more flat profile than the current clearing. This reason is probably because of the more complex shape of the current clearing.

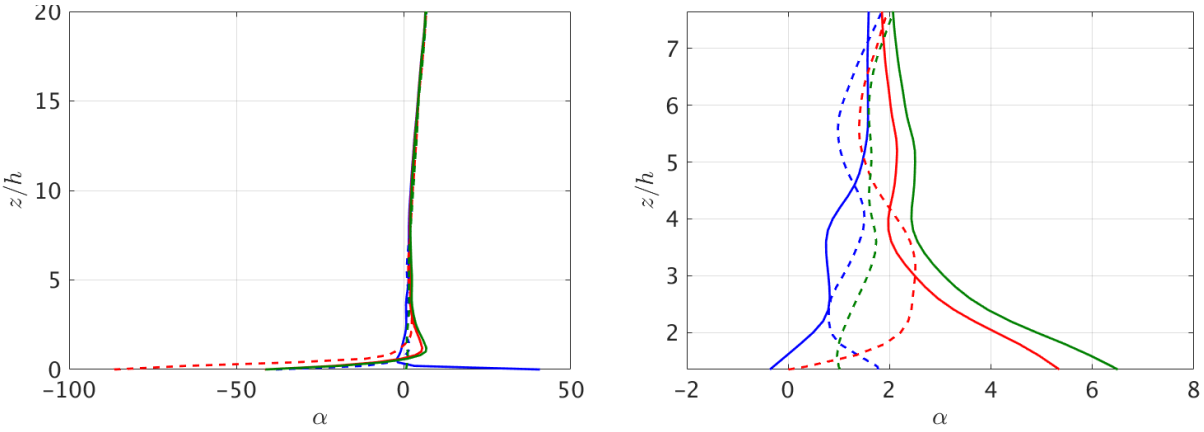

Figure 2.11: α from atmospheric boundary layer simulations at location of the wind turbine to the left and a zoom in rotor plane to the right. —: Wind turbine 1 in homogeneous forest, - -: Wind turbine 2 in homogeneous forest, —: Wind turbine 1 in current clearing, - -: Wind turbine 2 in current clearing, —: Wind turbine 1 in extended clearing, - -: Wind turbine 2 in extended clearing, —■—: Measurements

2.1.3 FAST simulations

The electrical generator power from FAST from the different wind turbines is seen in table 2.1. The first row in table 2.1 $\langle U \rangle^3$ shows OpenFOAM simulations without any turbines i.e. atmospheric boundary layer simulations. Where $\langle U \rangle^3$ is evaluated at the rotor plane. The second row presents OpenFOAM coupled to FAST simulations with only wind turbine 2 and the last row is from OpenFOAM coupled to FAST simulations in which both wind turbines are included. In order to facilitate comparison between homogeneous forest, current clearing and extended clearing the numbers at each line are related to wind turbine 2 in the homogeneous forest. For the atmospheric boundary layer simulation the power is estimated from the one dimensional momentum theory. For the first wind turbine FAST estimates an higher power than the atmospheric boundary layer simulations. No measurements were available for validation but due to the higher complexity of FAST, these results are assumed to be more correct than the atmospheric boundary layer estimate of power. The estimated power for the second wind turbine is the highest in all the atmospheric simulations followed by the simulations with only the second wind turbine and the simulations with both the wind turbines always give the lowest power estimate. This decrease in power of the second wind turbine in the simulations with both wind turbines compared to only one wind turbine shows that the first wind turbine has some effect on the second wind turbine when the wind is blowing from the south. For the first wind turbine all the simulations show the same trend. This is also the case for the second wind turbine of the current clearing. But for the second wind turbine in the extended clearing both the FAST simulations show that the power is lower than the second wind turbine in the homogeneous forest whereas the atmospheric boundary

layer simulation show the opposite. This show the complexity of the problem and the importance of the FAST coupling.

Electrical Generator Power	Homogeneous forest		Current clearing		Extended clearing	
	Turbine 1 (%)	Turbine 2 (%)	Turbine 1 (%)	Turbine 2 (%)	Turbine 1 (%)	Turbine 2 (%)
$\langle U \rangle^3$	+6.9	0.0	+7.0	+4.3	+7.2	+1.2
FAST, Only Turbine 2		0.0		+3.8		-2.6
FAST, Both Turbines	+8.6	0.0[a]	+8.5	+3.0	+8.5	-3.5

Table 2.1: $\langle U \rangle^3$ from the one dimensional momentum theory from atmospheric boundary layer simulations. Time averaged electrical generator power from simulations with wind turbines. [a]Wind turbine 2 in the homogeneous forest when both wind turbines are in the simulation is 3.3% higher than when only wind turbine 2 is in the simulation.

The bending moment of the rotor has also been investigated using FAST. The time averaged rotor bending around the x-axis i.e. rotor torque can be seen in table 2.2. Because of the close relation between power and torque the trends are the same as for the electrical generator power seen in table 2.1.

Rotor torque	Homogeneous forest		Current clearing		Extended clearing	
	Turbine 1 (%)	Turbine 2 (%)	Turbine 1 (%)	Turbine 2 (%)	Turbine 1 (%)	Turbine 2 (%)
FAST, Only Turbine 2		0.0		+2.6		-1.8
FAST, Both Turbines	+5.6	0.0[a]	+5.5	+2.0	+5.5	-2.4

Table 2.2: Time averaged rotor torque i.e. rotor bending moment around the x-axis. [a]Wind turbine 2 in the homogeneous forest when both wind turbines are in the simulation is 2.3% higher than when only wind turbine 2 is in the simulation.

To evaluate the fatigue loads the rain flow counting algorithm is used [23]. For the rotor torque it can be seen in fig. 2.12. The fatigue loading is more or less the same for all the wind turbines both when the first wind turbines are and are not included in the simulations. But the load range of the rotor torque is much lower than for the rotor bending around the y-axis as can be seen in fig. 2.13 and around the z-axis as can be seen in fig. 2.14. Hence the rotor torque is not a limiting factor.

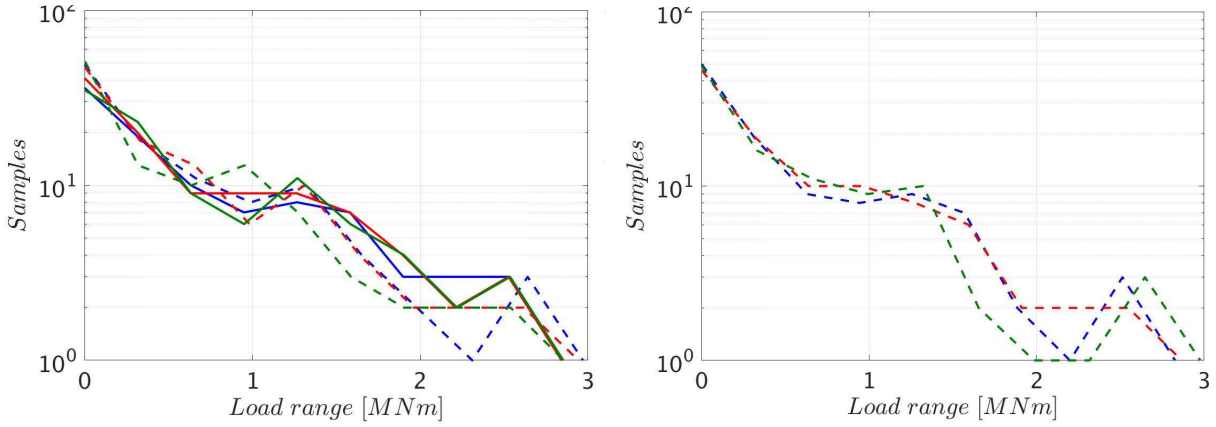

Figure 2.12: Rain flow of rotor torque i.e. rotor bending moment around the x-axis. Both wind turbines to the left and only wind turbine 2 to the right. —: Wind turbine 1 in homogeneous forest, - - -: Wind turbine 2 in homogeneous forest, —: Wind turbine 1 in current clearing, - - -: Wind turbine 2 in current clearing, —: Wind turbine 1 in extended clearing, - - -: Wind turbine 2 in extended clearing

For the rotor bending moment around the y-axis the RMS values are evaluated and presented in table 2.3. The reason for the difference in result for the first wind turbine in the homogeneous forest compared to the current and extended clearings is because the wind turbine is located on the edge of the forest in the clearing cases. This flattens the velocity profile in the region over the clearing and thus decreases the rotor bending moment around the y-axis. Comparing the second wind turbine for the different cases show that the current clearing has somewhat lower rotor bending moment around the y-axis than the wind turbine in the homogeneous forest. Looking at the horizontal velocity in fig. 2.5 it can be seen that the current clearing has a somewhat flatter velocity profile except in the lowest part of the rotor location compared to the homogeneous forest. The extended clearing in the location of wind turbine 2 has the lowest bending moment around the y-axis of them all. It can also be seen that the second wind turbine has the flattest velocity profile i.e. the lowest wind shear seen in fig. 2.5.

Rotor bending moment around y-axis	Homogeneous forest		Current clearing		Extended clearing	
	Turbine 1 (%)	Turbine 2 (%)	Turbine 1 (%)	Turbine 2 (%)	Turbine 1 (%)	Turbine 2 (%)
FAST, Only Turbine 2		0.0		-0.5		-5.0
FAST, Both Turbines	+2.4	0.0[a]	+1.0	-0.9	+1.0	-5.0

Table 2.3: RMS of rotor bending moment around the y-axis. [a]Wind turbine 2 in the homogeneous forest when both wind turbines are in the simulation is 0.2% higher than when only wind turbine 2 is in the simulation.

Consider the fatigue loads in fig. 2.13 when only the second wind turbine is included. The general trend is that the homogeneous forest has the highest loadings followed by the current clearing and the extended clearing has the lowest. When both wind turbines are included the

simulations it gets more difficult to distinguish the results. But the second wind turbine in the extended clearing is generally the one with the lowest loading range.

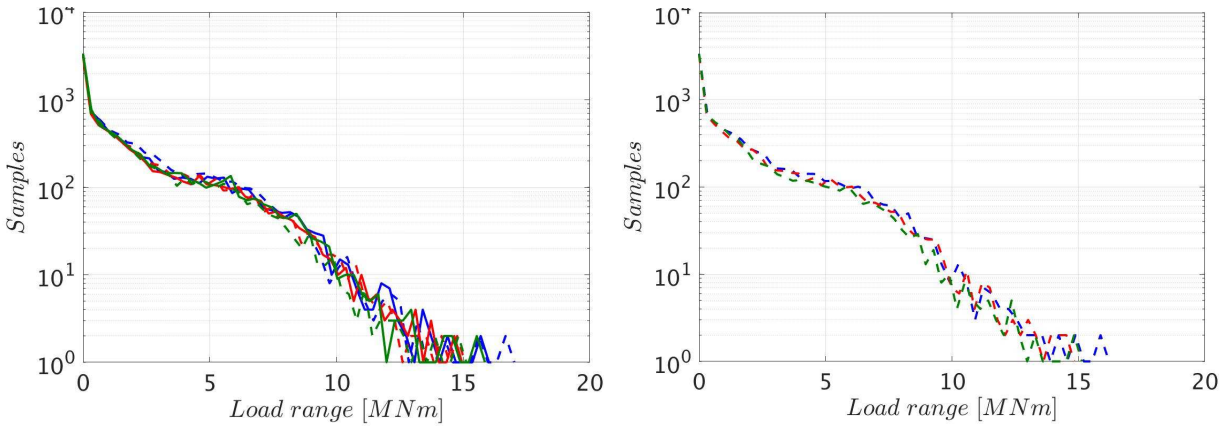

Figure 2.13: Rain flow of rotor bending moment around the y-axis. Both wind turbines to the left and only wind turbine 2 to the right. —: Wind turbine 1 in homogeneous forest, - - -: Wind turbine 2 in homogeneous forest, —: Wind turbine 1 in current clearing, - - -: Wind turbine 2 in current clearing, —: Wind turbine 1 in extended clearing, - - -: Wind turbine 2 in extended clearing

The RMS of the rotor bending around the z-axis is presented in table 2.4. The trends are the same as for the rotor bending moment around the y-axis. For the first wind turbines also the moment around the z-axis decreases when it is located in the forest edge compared to in a homogeneous forest. The second wind turbine in the current clearings has slightly lower moment around the z-axis than the second wind turbine in the homogeneous forest. It appears that the non-uniform in the $\bar{v}$ velocity seen in fig. 2.4 caused by the forest edge has favourable effects. Again the second wind turbines in the extended clearing clearly has the lowest moment around the z-axis.

Rotor bending moment around z-axis	Homogeneous forest		Current clearing		Extended clearing	
	Turbine 1 (%)	Turbine 2 (%)	Turbine 1 (%)	Turbine 2 (%)	Turbine 1 (%)	Turbine 2 (%)
FAST, Only Turbine 2		0.0		-1.0		-5.2
FAST, Both Turbines	+2.8	0.0[a]	+1.4	-0.8	+1.1	-5.0

Table 2.4: RMS of rotor bending moment around the z-axis. [a]Wind turbine 2 in the homogeneous forest when both wind turbines are in the simulation is 0.3% lower than when only wind turbine 2 is in the simulation.

The fatigue loads of the rotor bending moment around the z-axis presented in fig. 2.14 show that the trends are the same as for the rotor bending moment around the y-axis.

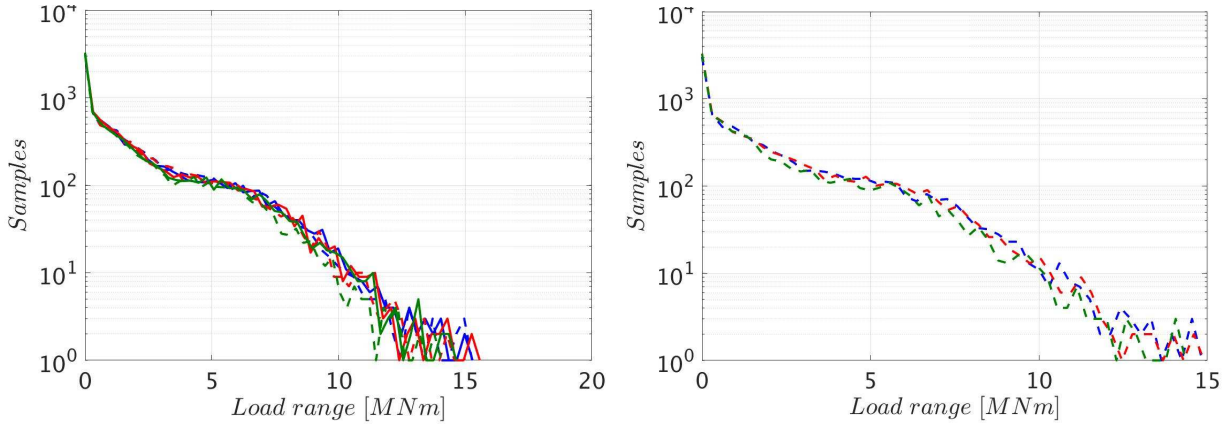

Figure 2.14: Rain flow of rotor bending moment around the z-axis. Both wind turbines to the left and only wind turbine 2 to the right. —: Wind turbine 1 in homogeneous forest, - - : Wind turbine 2 in homogeneous forest, —: Wind turbine 1 in current clearing, - - : Wind turbine 2 in current clearing, —: Wind turbine 1 in extended clearing, - - : Wind turbine 2 in extended clearing

The yaw bearing is fixed in the simulations and the bending moment is here investigated. The bending moment around the x-axis is given in table 2.5 and also here the close relation to the electrical power and the rotor torque is seen because the trends are the same.

Yaw bearing moment around x-axis	Homogeneous forest		Current clearing		Extended clearing	
	Turbine 1 (%)	Turbine 2 (%)	Turbine 1 (%)	Turbine 2 (%)	Turbine 1 (%)	Turbine 2 (%)
FAST, Only Turbine 2		0.0		+2.5		-1.9
FAST, Both Turbines	+5.5	0.0[a]	+5.4	+2.0	+5.4	-2.5

Table 2.5: Time averaged yaw bearing moment around x-axis. [a]Wind turbine 2 in the homogeneous forest when both wind turbines are in the simulation is 2.2% higher than when only wind turbine 2 is in the simulation.

The fatigue loads is seen in fig. 2.15 for the yaw bearing moment around the x-axis. As seen for the rotor bending moment, the yaw bearing moment around the x-axis is the lowest of the three and thereby not the limiting factor when comparing to the y-axis seen in fig. 2.16 and the z-axis seen in fig. 2.17.

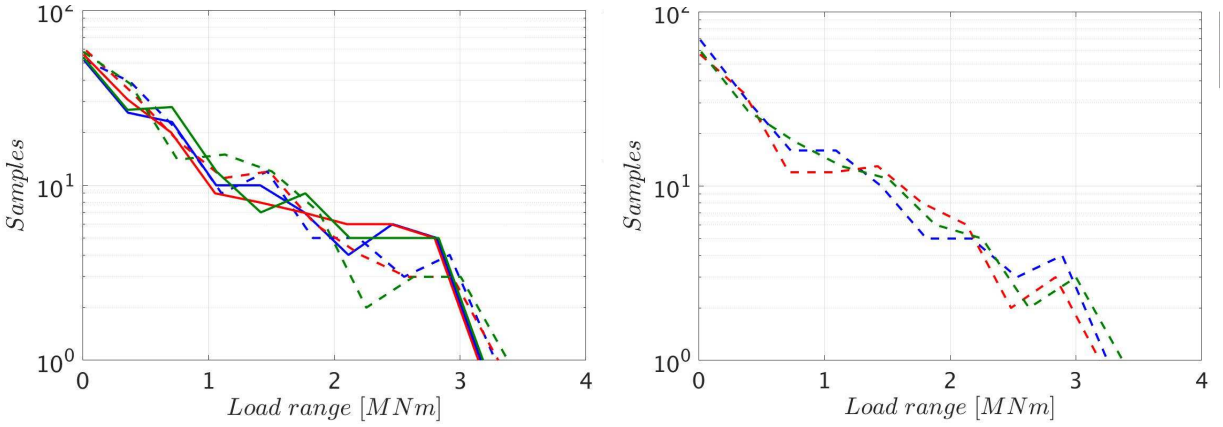

Figure 2.15: Rain flow of yaw bearing moment around the x-axis. Both wind turbines to the left and only wind turbine 2 to the right. —: Wind turbine 1 in homogeneous forest, - - -: Wind turbine 2 in homogeneous forest, —: Wind turbine 1 in current clearing, - - -: Wind turbine 2 in current clearing, —: Wind turbine 1 in extended clearing, - - -: Wind turbine 2 in extended clearing

For the yaw bearing bending around the y-axis the time averaged values can be seen in table 2.3. Here the two wind turbines in the homogeneous forest show rather similar values. The difference between wind turbine 1 and 2 increases as the clearing between them increases. When analysing wind turbine 2 with and without wind turbine 1 in the simulations with a clearing, the yaw bearing moment around the y-axis always increases by approximately 2% for all cases when wind turbine 1 is included i.e. wind turbine 1 has a negative effect on wind turbine 2.

Yaw bearing moment around y-axis	Homogeneous forest		Current clearing		Extended clearing	
	Turbine 1 (%)	Turbine 2 (%)	Turbine 1 (%)	Turbine 2 (%)	Turbine 1 (%)	Turbine 2 (%)
FAST, Only Turbine 2		0.0		-5.1		-20.2
FAST, Both Turbines	-0.6	0.0[a]	-5.1	-3.6	-5.8	-18.7

Table 2.6: Time averaged yaw bearing moment around y-axis. [a]Wind turbine 2 in the homogeneous forest when both wind turbines are in the simulation is 1.3% higher than when only wind turbine 2 is in the simulation.

The fatigue loads seen in fig. 2.16 follows the same trends as seen before, with wind turbine 2 in the extended forest having the lowest fatigue load.

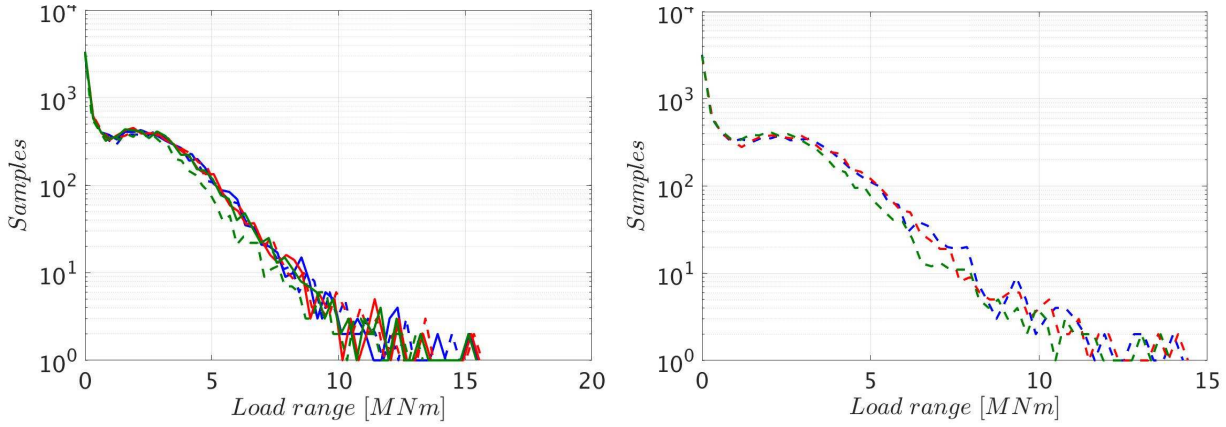

Figure 2.16: Rain flow of yaw bearing moment around the y-axis. Both wind turbines to the left and only wind turbine 2 to the right. —: Wind turbine 1 in homogeneous forest, - -: Wind turbine 2 in homogeneous forest, —: Wind turbine 1 in current clearing, - -: Wind turbine 2 in current clearing, —: Wind turbine 1 in extended clearing, - -: Wind turbine 2 in extended clearing

The time averaged moment around the z-axis for the yaw bearing can be seen in table 2.7. Here wind turbine 2 in the current clearing has the lowest value. When looking at fig. 2.4 this is the wind turbine which experiences the largest variations in the $\bar{v}$ velocity. This shows that the shape of the clearing can have a positive influence on the wind turbines located close to a clearing.

Yaw bearing moment around z-axis	Homogeneous forest		Current clearing		Extended clearing	
	Turbine 1 (%)	Turbine 2 (%)	Turbine 1 (%)	Turbine 2 (%)	Turbine 1 (%)	Turbine 2 (%)
FAST, Only Turbine 2		0.0		-14.1		-1.0
FAST, Both Turbines	-6.2	0.0[a]	-5.9	-23.7	-4.6	-7.1

Table 2.7: Time averaged yaw bearing moment around z-axis. [a]Wind turbine 2 in the homogeneous forest when both wind turbines are in the simulation is 9.8% lower than when only wind turbine 2 is in the simulation.

Also for the fatigue loads of the yaw bearing around the z-axis seen in fig. 2.17, it is found that wind turbine 2 in the extended clearing is displaying the smallest load. This is somewhat surprising because of the large decrease in time averaged value of wind turbine 2 in the current clearing seen in table 2.7. This shows the importance of including not only the time averaged values but also the fatigue loads in the analysis.

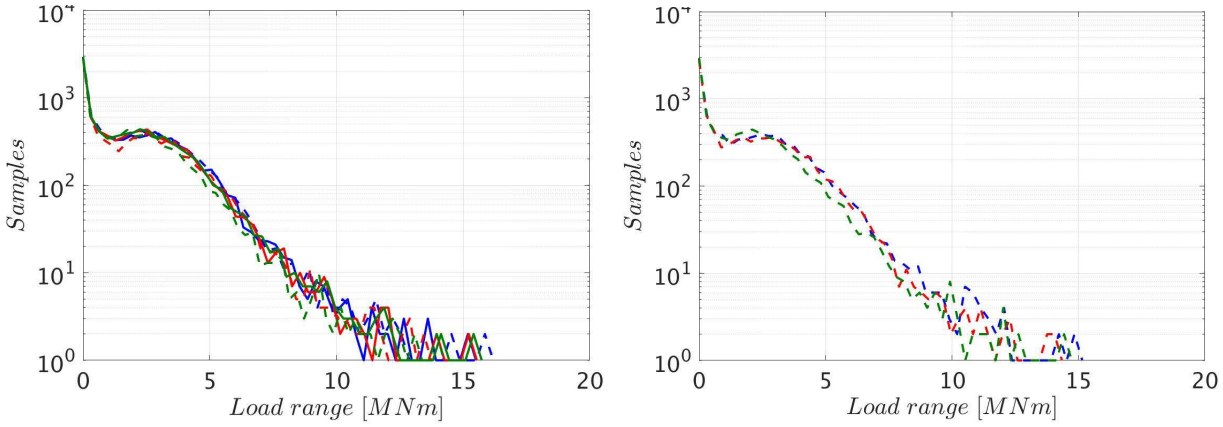

Figure 2.17: Rain flow of yaw bearing moment around the z-axis. Both wind turbines to the left and only wind turbine 2 to the right. —: Wind turbine 1 in homogeneous forest, - - -: Wind turbine 2 in homogeneous forest, —: Wind turbine 1 in current clearing, - - -: Wind turbine 2 in current clearing, —: Wind turbine 1 in extended clearing, - - -: Wind turbine 2 in extended clearing

The in-plane and out-of-plane bending moment at the blade root is also investigated. The time averaged values of the in-plane bending moment can be seen in fig. 2.8 and for the out-of-plane in fig. 2.9. Both show the same trends as for the electrical generator power and the rotor torque. This is logical because if the loads on the blades increase so does also the rotor torque.

In-plane bending moment at blade root	Homogeneous forest		Current clearing		Extended clearing	
	Turbine 1 (%)	Turbine 2 (%)	Turbine 1 (%)	Turbine 2 (%)	Turbine 1 (%)	Turbine 2 (%)
FAST, Only Turbine 2		0.0		+2.6		-1.8
FAST, Both Turbines	+5.5	0.0[a]	+5.5	+2.0	+5.5	-2.3

Table 2.8: Time averaged in-plane bending moment at blade root. [a]Wind turbine 2 in the homogeneous forest when both wind turbines are in the simulation is 2.3% higher than when only wind turbine 2 is in the simulation.

For the lower fatigue load range, wind turbine 2 in the extended clearing shows the lowest values seen in fig. 2.18. But for the higher loads they all give approximately the same results.

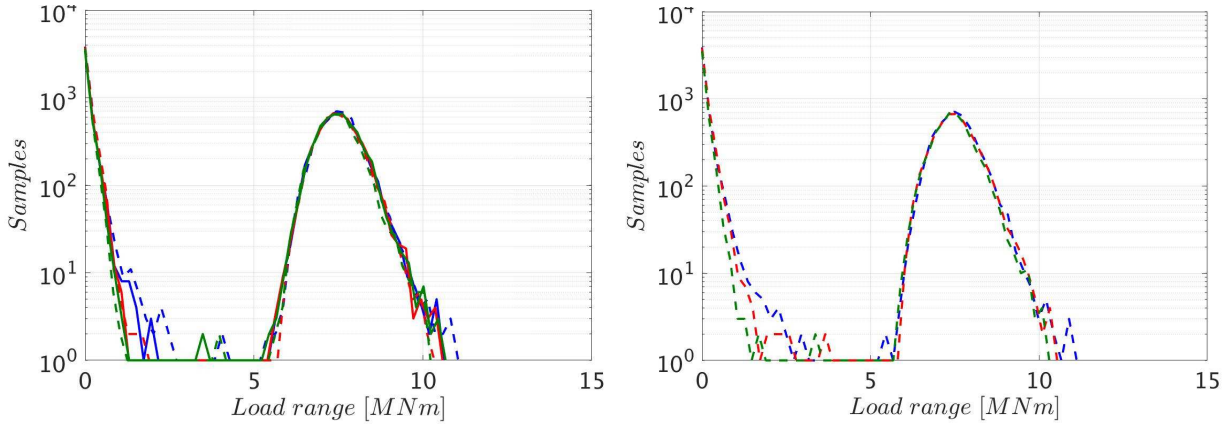

Figure 2.18: Rain flow of Blades in-plane moment around the x-axis. Both wind turbines to the left and only wind turbine 2 to the right. —: Wind turbine 1 in homogeneous forest, - - : Wind turbine 2 in homogeneous forest, —: Wind turbine 1 in current clearing, - - : Wind turbine 2 in current clearing, —: Wind turbine 1 in extended clearing, - - : Wind turbine 2 in extended clearing

Out-of-plane bending moment at blade root	Homogeneous forest		Current clearing		Extended clearing	
	Turbine 1 (%)	Turbine 2 (%)	Turbine 1 (%)	Turbine 2 (%)	Turbine 1 (%)	Turbine 2 (%)
FAST, Only Turbine 2		0.0		+3.0		-0.7
FAST, Both Turbines	+5.2	0.0[a]	+5.2	+2.3	+5.2	-1.3

Table 2.9: Time averaged out-of-plane bending moment at blade root. [a]Wind turbine 2 in the homogeneous forest when both wind turbines are in the simulation is 2.3% higher than when only wind turbine 2 is in the simulation.

The fatigue loads for the out-of-plane moment at the blade root can be seen in fig. 2.19. Here wind turbine 2 in the extended clearing shows the lowest fatigue loads.

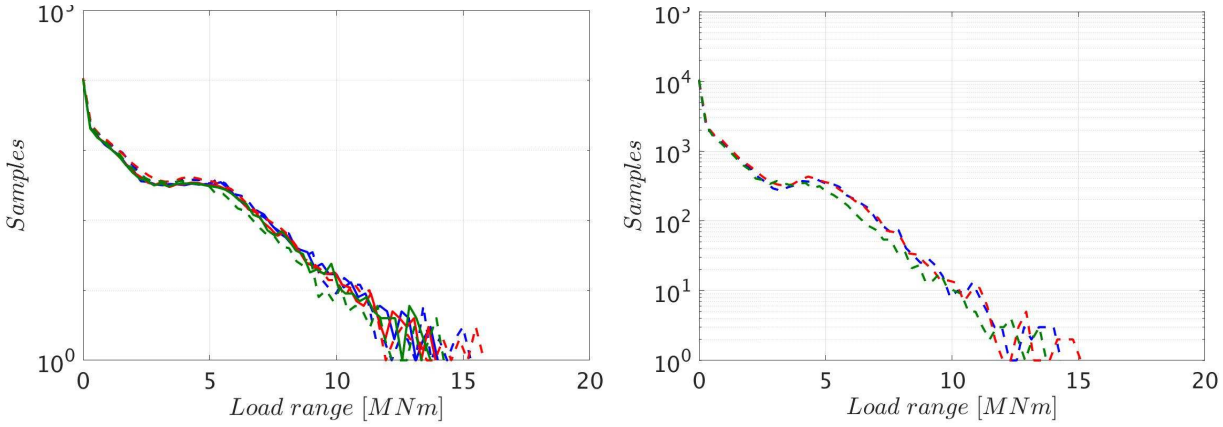

Figure 2.19: Rain flow of Blades out-plane moment around the y-axis. Both wind turbines to the left and only wind turbine 2 to the right. —: Wind turbine 1 in homogeneous forest, - -: Wind turbine 2 in homogeneous forest, —: Wind turbine 1 in current clearing, - -: Wind turbine 2 in current clearing, —: Wind turbine 1 in extended clearing, - -: Wind turbine 2 in extended clearing

The tower base moment around the y-axis is also investigated and the time averaged values can be seen in table 2.10. These results also have the same trend as the electrical generator power.

Tower base moment around y-axis	Homogeneous forest		Current clearing		Extended clearing	
	Turbine 1 (%)	Turbine 2 (%)	Turbine 1 (%)	Turbine 2 (%)	Turbine 1 (%)	Turbine 2 (%)
FAST, Only Turbine 2		0.0		+2.8		-2.2
FAST, Both Turbines	+5.1	0.0[a]	+4.9	+2.2	+4.9	-2.7

Table 2.10: Time averaged tower base moment around y-axis. [a]Wind turbine 2 in the homogeneous forest when both wind turbines are in the simulation is 2.4% higher than when only wind turbine 2 is in the simulation.

Consider the fatigue loads for the tower base moment in fig. 2.20 wind turbine 2 in the extended forest is found to be only slightly favourable compared to the other cases at low load ranges.

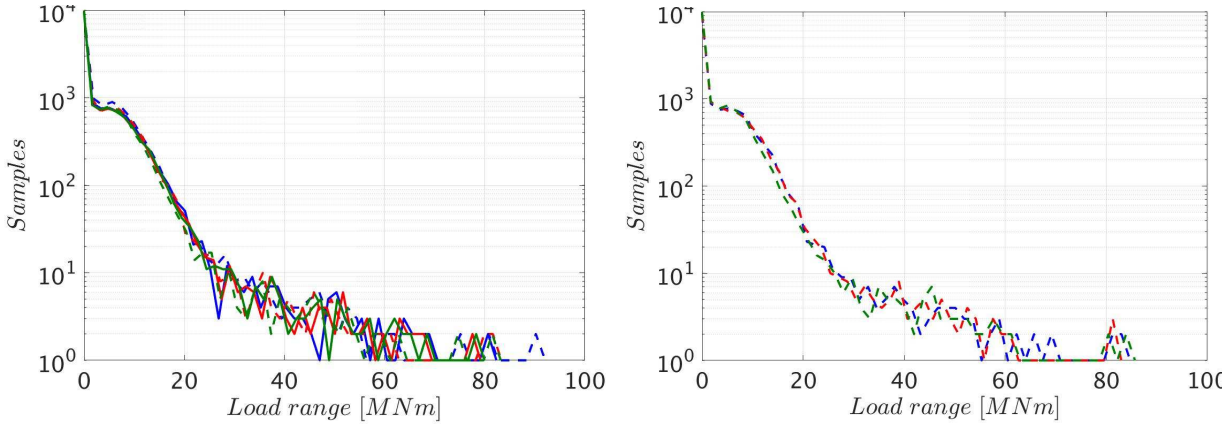

Figure 2.20: Rain flow of tower base pitching moment around the y-axis. Both wind turbines to the left and only wind turbine 2 to the right. —: Wind turbine 1 in homogeneous forest, - - : Wind turbine 2 in homogeneous forest, —: Wind turbine 1 in current clearing, - - : Wind turbine 2 in current clearing, —: Wind turbine 1 in extended clearing, - - : Wind turbine 2 in extended clearing

Chapter 3

Future outlook

Interesting focus points to study in the future related to this work is to optimize the clearing and wind turbine location in relation to it in order to obtain higher electrical power and lower fatigue loads. This study covers only the Ryningsnäs site but in the future other sites will also be studied in order to see if the trends remain the same as what has been shown in this work. The terrain of the site might have an effect on the wind turbines together with the clearing, which is a phenomena that also would be interesting to unveil. The present work covers only neutral stratification but unstable and stable stratification will also be studied. SOWFA used in this work is two way coupled to FAST but the difference to a one way coupled simulation setup is still unknown.

Further along in the future other interesting focus points might be studied. The new standard for the tower height of wind turbines installed in forests are 130m tower height compared the 90m of the 5MW NREL wind turbine used in this work. By studying the new standard of tower height one can advice wind farms developer of new wind farms how to optimize the output from the wind turbines and minimize the fatigue loads. The 5MW wind turbine with its 90m tower is however still relevant to help current wind farms perform better. NREL has recently released a new SOWFA version using FAST version 8. This will allow for the use of the new modularized framework in FAST. If this new version will be shown to have sufficient benefits over the older version, this version will be used instead.

Bibliography

[1] B. Nebenfuhr and L. Davidson. Influence of a forest canopy on the neutral atmospheric boundary layer a les study, 2014.

[2] M. Zendehbad, N. Chokani, and R. Abhari. Impact of forested fetch on energy yield and maintenance of wind turbines. *Renewable Energy*, 96:548–558, 2016.

[3] E. Mueller, W. Mell, and A. Simeoni. Large eddy simulation of forest canopy flow for wildland fire modeling. *Canadian Journal of Forest Reasearch*, 44(12):1534–1544, 2014.

[4] E. Dellwik, F. Bingl, and J. Mann. Flow distortion at a dense forest edge. *Quarterly Journal of the Royal Meteorological Society*, 140:676–686, 2014.

[5] S. Dupont and Y. Brunet. Coherent structures in canopy edge flow: A large-eddy simulation study. *Journal of Fluid Mechanics*, 630(7):93–128, 2009.

[6] S. Dupont, J.-M. Bonnefond, M. R. Irvine, E. Lamaud, and Y. Brunet. Long-distance edge effects in a pine forest with a deep and sparse trunk space: In situ and numerical experiments. *Agricultural and Forest Meteorology*, 151(3):328–344, 2011.

[7] W. Klaassen, P. van Breugel, E. Moors, and J. Nieveen. Increased heat fluxes near a forest edge. *Theoretical and Applied Climatology*, 72(3-4):231–243, 2002.

[8] S. Dupont and Y. Brunet. Edge flow and canopy structure: A large-eddy simulation study. *Boundary-Layer Meteorology*, 126(1):51–71, 2008.

[9] A. Glazunov and V. Stepanenko. Large-eddy simulation of stratified turbulent flows over heterogeneous landscapes. *Atmospheric and Oceanic Physics*, 51(4):403–415, 2015.

[10] D. D. Baldocchi and T. D. Meyers. Turbulence structure in a deciduous forest. *Boundary-Layer Meteorology*, 43:345–364, 1988.

[11] S. Dupont and Y. Brunet. Simulation of turbulent flow in an urban forested park damaged by a windstorm. *Boundary-Layer Meteorology*, 120(1):133–161, 2006.

[12] M. Churchfield, S. Lee, and P. Moriarty. Overview of the simulator of offshore wind farm application. Webinar, NREL, 2012.

[13] R. Shaw and U. Shumann. Large-eddy simulation of turbulent flow above and within a forest. *Boundary-Layer Meteorology*, 61(1):47–64, 1992.

[14] B. Lalic and D. Mihailovic. An empirical relation describing leaf area density inside the forest for environmental modeling. *Journal of Applied Meteorology*, 43(4):641–645, 2004.

[15] N. Troldborg. Actuator line modeling of wind tubine wakes. Ph.d. thesis, Technical University of Denmark, 2008.

[16] R. Mikkelsen. Actuator disc methods applied to wind turbines. Ph.d. thesis, Technical University of Denmark, 2003.

[17] L. Martinez, S. Leonardi, M. Churchfield, and P. Moriarty. A comparison of actuator disk and actuator line wind turbine models and best practices for their use, 2012.

[18] J.N. Sørensen and W.Z. Shen. Numerical modeling of wind turbine wakes. *Journal of Fluids Engineering*, 124:393–399, 2002.

[19] J.N. Sørensen, W.Z. Shen, and X. Munduate. Analysis of wake states by a full-field actuator disc model. *Wind Energy*, 1:73–88, 1998.

[20] J. Matsfelt. Actuator turbine models and trailing edge flow: implementation in an in-house code. Master thesis, Chalmers University of Technology, 2015.

[21] J. Smagorinsky. General circulation experiments with the primitive equations. *Monthly Weather Review*, 91:99–164, 1963.

[22] U. Schumann. Subgrid-scale model for finite-difference simulations of turbulent flow in plane channels and annuli. *Journal of Computational Physics*, 18:76–404, 1975.

[23] ASTM. Standard practices for cycle counting in fatigue analysis. Technical report, American Society for Testing and Materials, 1985.

[24] J. Jonkman, S. Butterfield, W. Musial, and G. Scott. Definition of a 5-mw reference wind turbine for offshore system development. Technical report, NREL, 2009.

[25] H. Bergstrom, H. Alfredsson, J. Arnqvist, I. Carlen, E. Dellwik, J. Fransson, H. Ganander, M. Mohr, A. Segalini, and S. Soderberg. Wind power in forests: wind and effects on loads. Vindforsk report, Uppsala, 2013.